Available online at www.sciencedirect.com
ScienceDirect
Physics Procedia 1 (2008) 485–504
Physics Procedia
www.elsevier.com/locate/procedia

Proceedings of the Seventh International Conference on Charged Particle Optics

Electron optics for low energy electron microscopy

Marian Mankos[a]*, David Adler[a], Lee Veneklasen[‡] and Eric Munro[b]

[a]*KLA-Tencor, 160 Rio Robles, San Jose, CA, U.S.A.*
[b]*Munro's Electron Beam Software Ltd., 14 Cornwall Gardens, London SW7 4AN, England*
[‡] *In memory of L. Veneklasen's contribution*

Received 9 July 2008; received in revised form 9 July 2008; accepted 9 July 2008

Abstract

Novel electron-optical components and concepts aiming at improving the throughput and extending the applications of a low energy electron microscope (LEEM) are elucidated: an immersion magnetic field in the objective lens and its implications for the illumination optics, a dual electron beam illumination approach, and imaging modes with tilted illumination. In an immersion magnetic objective lens, electrons do not form a sharp crossover in the back-focal plane, which substantially reduces e-e interactions and the associated blur. The resulting limited field of view of the immersion objective lens in mirror mode can be eliminated by immersing the cathode of the electron gun in a magnetic field. A dual beam approach, where two beams with different landing energies illuminate the field of view, is used to mitigate the charging effects when the LEEM is used to image insulating surfaces. We have experimentally demonstrated that the negative charging effect, created by a partially absorbed mirror beam, is compensated by the positive charging effect of the secondary beam with a net electron yield exceeding 1. On substrates illuminated with a tilted beam near glancing incidence, large shadows are formed on even the smallest topographic features, easing their detection. On magnetic substrates, the magnetic flux leaking above the surface can be detected with tilted illumination and used to image domain walls with high contrast.

PACS: 68.37.Nq; 41.85.-p

Keywords: Low energy electron microscope (LEEM); Electron beam inspection system; Electron optics

1. Introduction

As semiconductor device feature sizes continue to shrink, scanning electron beam tools face an increasing challenge due to their relatively low throughput: the number of pixels to be examined on a wafer results in inspection times that exceed practical limits. One of the possible approaches to circumvent this problem is to replace the serial acquisition process of scanning electron microscopes with a parallel scheme, where all the image pixels of interest on the surface are acquired in parallel on a scintillating screen and further processed on a computer. A LEEM, optimized for high throughput, i.e. large beam currents and field sizes, is ideally suited for this application. In a LEEM [1,2], electrons illuminating the sample have energies ranging from a few hundred eV to

* Corresponding author. Tel.: +1-408-875-1510
E-mail address: marian.mankos@kla-tencor.com

doi:10.1016/j.phpro.2008.07.131

near zero eV, depending on the substrate bias. When the wafer is biased positively with respect to the electron source, the electrons scatter at or near the surface, and either reflect back from the sample, undergoing low energy electron diffraction, or generate secondary electrons, provided the bias and therefore kinetic energy of the illuminating electrons is large enough (few tens to hundreds eV). When the substrate is biased slightly negative (~1V) with respect to the electron source, the illuminating electrons are reflected above the surface, without hitting the surface. This imaging mode is also known as mirror electron microscopy (MEM).

The fact that electrons reflect back and travel along the path of the incident beam poses a major challenge in the design of an electron microscope. Since independent control of the illumination and projection is required, the optical axis is split by a magnetic sector field, a non-radially symmetric optical element. This requires a departure from the traditional design with a straight optical axis, resulting in a more complex optical design. We have adopted a design with a straight gun-to-screen axis. The four subsystems of the electron-optical column, the magnetic prism array, the illumination, objective and projective optics are shown in Fig. 1.

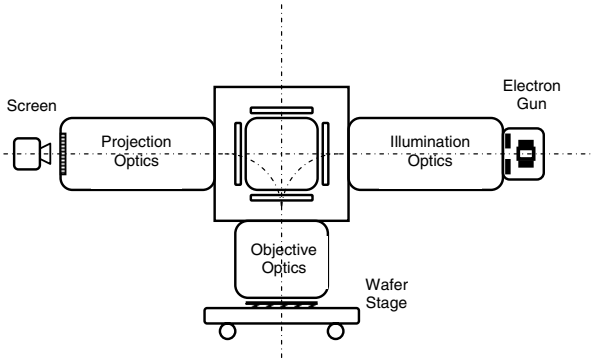

Fig. 1. Basic layout of LEEM optics.

The illuminating electrons are emitted from the surface of a flat cathode and accelerated to their final beam energy, forming a crossover inside the electron gun. The cathode temperature and extraction field determine the total beam emitted from the gun. The following condensor lenses form a zoom lens which maintains a focused image of the gun crossover at the illumination shape aperture, and allows varying the current illuminating the wafer and therefore determines the number of electrons/pixel reaching the detector. A further set of lenses is used to vary the current density at the wafer and therefore determines the size of the illuminated area. The magnetic prism array deflects the electron beam from the illumination optics into the objective optics. Below the magnetic prism array, the electron-optical components of the objective optics are common to the illumination and projection optics. The immersion cathode objective lens decelerates the electrons before they reach the substrate and illuminates the wafer surface with a nearly uniform beam. The electrostatic part of the objective lens creates an electric field of ~ 5 kV/mm at the substrate surface. In the opposite direction, i.e. upward from the substrate, the objective lens simultaneously forms a magnified image of the substrate surface using mirrored, secondary, backscattered or photoemission electrons. As the electrons reenter the prism array, they get deflected into the projection optics. The magnetic prism array is followed by a diffraction lens, which forms an image of the objective lens back-focal plane in the pupil aperture plane and simultaneously forms a magnified image of the wafer in the object plane of the projection zoom optics. The zoom section is followed by the final magnifying element of the projection optics, the final projector lens. The electron image formed at the scintillating screen is then viewed by a CCD camera and further processed on a computer.

The throughput is determined by the time required to deliver an electron dose that is required to provide a useful signal with sufficient signal-to-noise ratio, so it is proportional to the maximum total electron current. However, the large current required to deliver the needed throughput results in increased electron-electron (e-e) interactions, which blur the image and result in a loss of resolution. In this paper we evaluate the impact of high-throughput requirements on the electron-optical design of a LEEM. We introduce electron-optical components and concepts

aiming at improving the throughput, in particular an immersion magnetic field in the objective lens, a novel magnetic prism array, a dual electron beam illumination approach, and its implications for the illumination optics.

2. Magnetic immersion objective lens

In a cathode objective lens, the substrate forms the cathode, analogous to an emitter in a gun lens. The surface is biased at a high negative voltage (tens of kV), and immersed in a strong electrostatic field ranging from a few to 10 kV/mm. A magnified image of the substrate is formed using electrons that are generated by illuminating the surface of the substrate with photons or low-energy electrons. The extraction electrode is typically a planar electrode with an aperture hole in the center. The accelerating field forms a magnified virtual image of the substrate surface that is further magnified by the electrostatic or magnetic lens to form a magnified image of the surface, and then deflected into the projection optics by the magnetic prism array for further magnification. Cathode objective lenses were used in the past in a variety of electron microscopes, including low-energy electron microscopes [1,2], photoemission electron microscopes [3,4] and low-voltage scanning electron microscopes [5]. Increasingly, these lenses are finding applications in scanning electron beam tools used in the semiconductor industry [6-9].

Four types of cathode objectives with constant accelerating field were considered: decelerating and accelerating electrostatic, and combined magnetic immersion and non-immersion lenses. All lenses have an accelerating field of approximately 5 kV/mm at the substrate surface and for comparison operate at a beam energy of 20 kV. The geometry of the focusing electrodes and polepieces was chosen to give a practical lens design capable of forming a 4-5 times magnified image of reasonable size (few hundreds of μm) at a distance of 200 mm from the substrate. For our simulations, we use the IMAGE software package from MEBS Ltd. to evaluate the impact of e-e interactions. The software computes electron-optical properties by propagating bunches of particles through realistic electromagnetic fields by accurate direct ray-tracing. The beam blur is calculated typically for field sizes ranging from 50 μm x 50 μm to 500 μm x 500 μm and total beam currents ranging from 200 nA to 20 μA. The emission area has a square shape, with a uniform current density distribution. The angular intensity distribution is Lambertian, and the initial energy has a Maxwell-Boltzmann distribution peaked at 0.25 eV.

Increased throughput requires a large total beam current, which results in increased e-e interactions. The e-e interactions affect the imaging properties of the cathode objective lens by increasing the beam energy spread (Boersch effect), and introducing blur (trajectory displacement effect) and space charge defocus [10]. Both the Boersch effect, which increases the chromatic aberration contribution, and the trajectory displacement (Loeffler) effect, which shifts the electron positions and velocities, directly deteriorate the imaging quality of the lens and cannot be fully corrected. The space charge defocus, determined by the averaged charge density in the beam, results in a defocus of the image from the Gaussian plane and a change in magnification. The defocus can be corrected for a uniform charge distribution in an axially symmetric beam, by refocusing the lens [10,11]. For non-uniform charge density distributions, the divergent lens will have further aberrations [12].

A detailed analysis of both the electrostatic and the combined magnetic non-immersion lenses was presented earlier [13], so we will focus on the magnetic immersion objective lens. In general, the e-e interactions can be reduced for a given beam current in the cathode objective lens by increasing the illuminated area, which decreases the current density. The functional dependence of the e-e induced beam blur d_{ee} at the Gaussian focus plane upon beam current for an illumination area of 800 μm x 800 μm for the decelerating electrostatic and immersion and non-immersion magnetic lens is shown in Fig. 2. The immersion magnetic lens shows a significantly reduced effect of e-e interactions, in particular a blur d_{ee} of ~ 50 nm should be achievable for currents as high as 10 μA under these conditions. It also can be seen that the stronger the magnetic field at the substrate (i.e. smaller lens working distance d), the smaller the blur d_{ee}. For each current, the blur d_{ee} (referred to the substrate plane) due to e-e interactions is calculated by subtracting the blur d_0 at very low currents from the total blur d_t using a Gaussian quadrature, i.e. $d_{ee}^2 = d_t^2 - d_0^2$. At low currents (1 nA), all lenses are capable of achieving a total blur of approximately 70 nm at 20 keV. No pupil aperture is used so that all the electrons are detected.

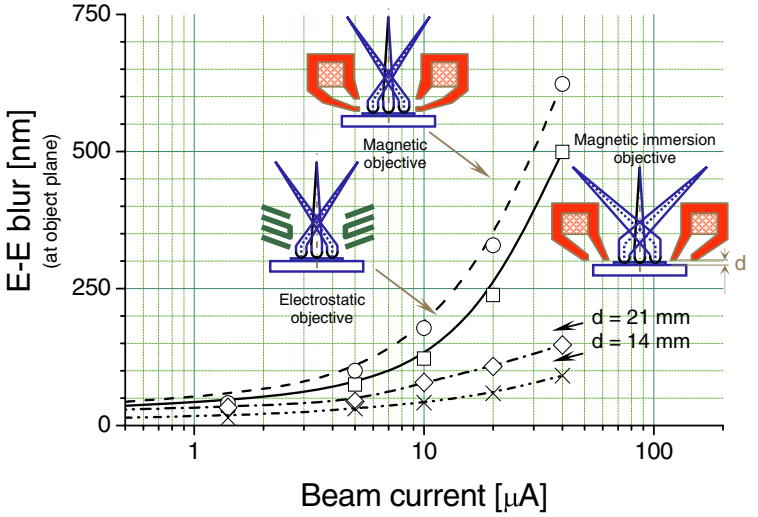

Fig. 2. Electron-electron interactions induced blur as a function of beam current for three types of cathode lenses.

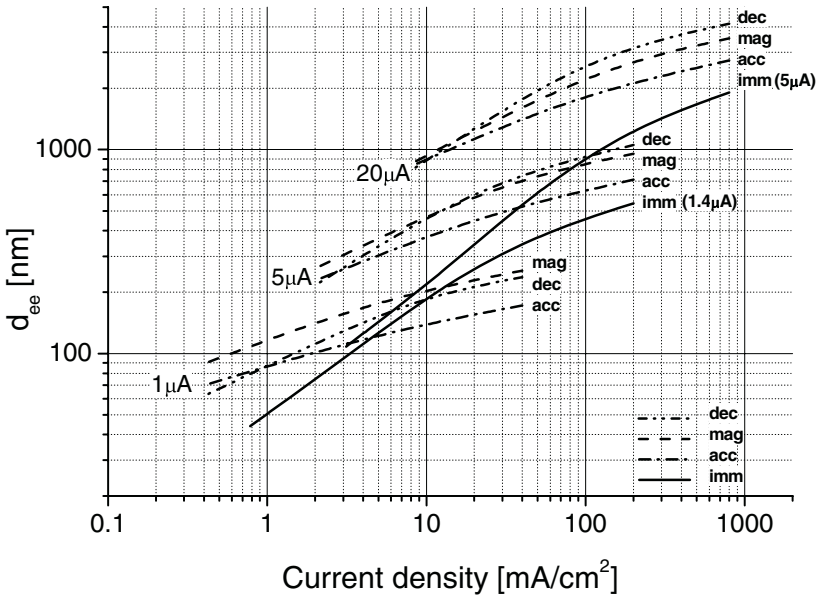

Fig. 3. Electron-electron interactions induced blur as a function of current density for four types of cathode lenses.

Fig. 3 shows the beam blur d_{ee} as a function of current density for the three conventional lens types with total beam currents ranging from 1 to 20 μA and compares it with the immersion lens for currents from 1.4 to 5 μA. The immersion magnetic lens displays a peculiar behavior at low current densities, qualitatively different form the other 3 lens types [13], resulting in further substantial reduction of the associated blur d_{ee}. This is due to the fact that electrons emitted from rest inside a magnetic field have a finite angular velocity when they emerge in the field free region which prevents the formation of a sharp, well defined crossover in the back-focal plane of the objective lens,

resulting in reduced e-e interactions. The crossover size becomes dependent upon the size of the illumination area, and increases with increasing flux density at the substrate. In such a lens, the e-e interactions-induced blur becomes independent of beam current at low current densities. This means that large currents can be used for imaging, provided the current density is kept below a threshold of approximately 10 mA/cm^2 (for this geometry at 20keV). Experimental data obtained on a LEEM operating at 25 keV and equipped with an immersion objective lens are shown in Fig. 4, showing no significant increase in blur for beam currents ranging from 0.5 to 3 μA.

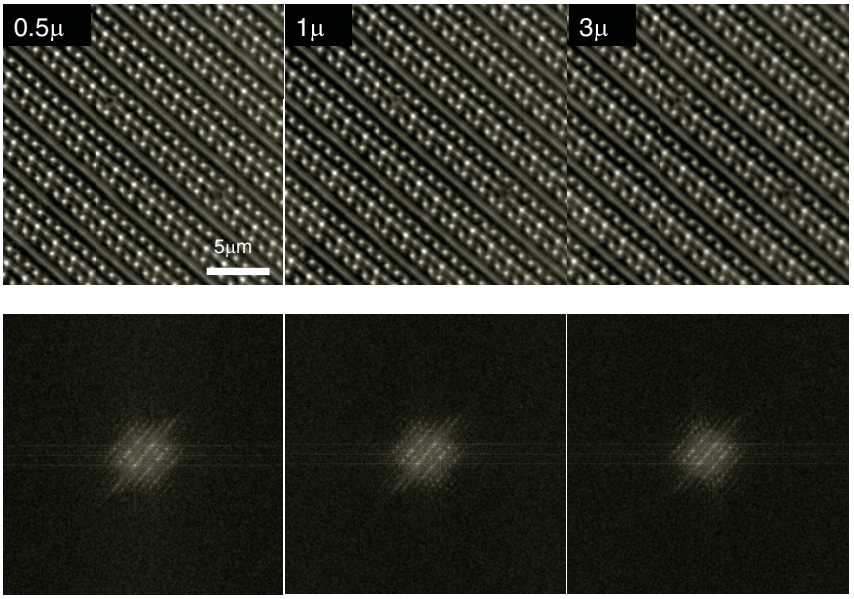

Fig. 4. Mirror images and their FFTs obtained with an immersion magnetic cathode lens for a range of beam currents, field of view 25μm x 25μm; sample: Aluminum-coated Si substrate with periodic, 100nm thick SiO_2 structures.

The immersion magnetic cathode lens has also a significant advantage when conventional geometric aberrations are considered. The contribution from off-axis aberrations, which can limit the available field size at the substrate, is illustrated in Fig. 5, which compares the 12-88% blur as function of field size obtained in a conventional electrostatic decelerating cathode lens and the immersion magnetic cathode lens. It can be seen from Fig. 5 that the immersion magnetic lens has very low field aberrations, allowing a significantly larger field of view.

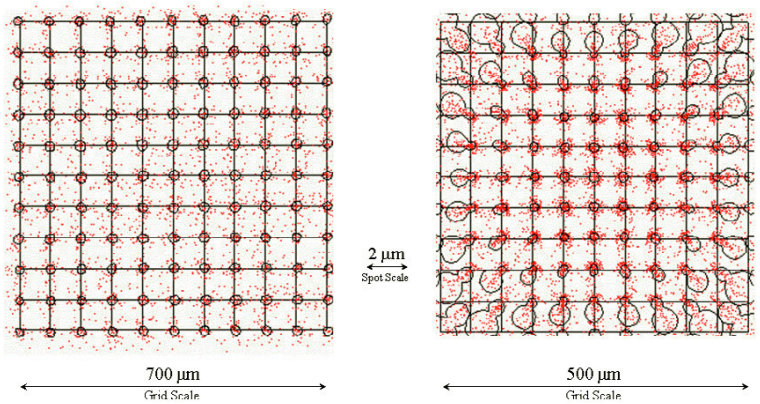

Fig. 5. Spot diagrams for an immersion magnetic (left) and electrostatic deceleration cathode lens.

3. Magnetic prism array

The electron-optical properties of the prism array strongly impact the design of the entire tool, since the physical size of the prism array determines the location of the image and diffraction planes. Unfortunately, the focusing properties of simple magnetic prisms differ considerably in the horizontal and vertical planes, giving rise to large astigmatism and distortion. Ideally, we need a magnetic prism with a net deflection of 90° which behaves like a set of round lenses and images simultaneously the real-space image of the sample and the diffraction pattern (back-focal plane of the objective lens, slit plane). This can be achieved in a close-packed magnetic prism array [14,15], consisting of a large, central square magnetic field, surrounded by several smaller regions where the magnetic field is about three times stronger and in the same direction (Fig.6). During each 90° deflection, the beam passes through an outer, inner, central, inner and outer sector. The inner and outer sectors are significantly shorter than the central sector. Each sector has an independent coil wound around it which allows the control of the magnetic flux density generated by each sector. A cross-section of the prism array, shown in Fig.7, shows the position of the individual coils and the magnetic flux density profile.

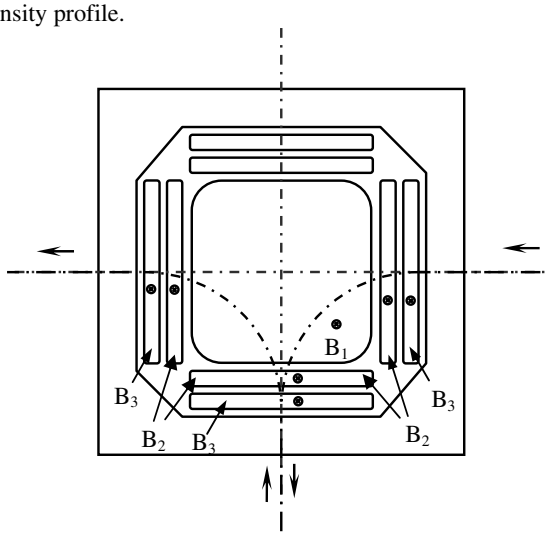

Fig. 6. Layout of the magnetic prism array.

We have used a dedicated software package developed by MEBS, Ltd. to calculate the properties of 90° prism arrays. In this package, prism arrays consisting of magnet regions held at different magnetic excitations and separated by gaps consisting of grooves parallel to the faces of the magnet can be evaluated. The fields are represented with the help of Schwartz-Christoffel transformations and the direct ray-tracing is done with a Runge-Kutta solution of the equations of motion. The program first computes the path of the optical axis through the magnet field for specified pole-piece excitations and then adjusts the pole-piece excitations to obtain exactly 90° bending of the optical axis.

Four fundamental paraxial rays are then computed – an imaging ray and a field ray in the bending plane, and an imaging ray and a field ray in the transverse plane. In general, the two imaging rays will not form a stigmatic image, and neither will the two field rays form a stigmatic focus. The program iteratively adjusts the pole-piece excitations and/or the magnet geometry in order to zero the astigmatic difference in the image and slit plane simultaneously, while keeping the axis bending angle 90°. Three degrees of freedom – i.e. three variable parameters in the design – are required to achieve the stigmatic focus at image plane and slit plane, with 90° bending. For this purpose, the variable parameters can include the spacing between the upper and lower polepieces, the gap widths, the gap positions and the pole-piece excitations. After stigmatic imaging has been achieved, the program computes the dispersion in the slit plane.

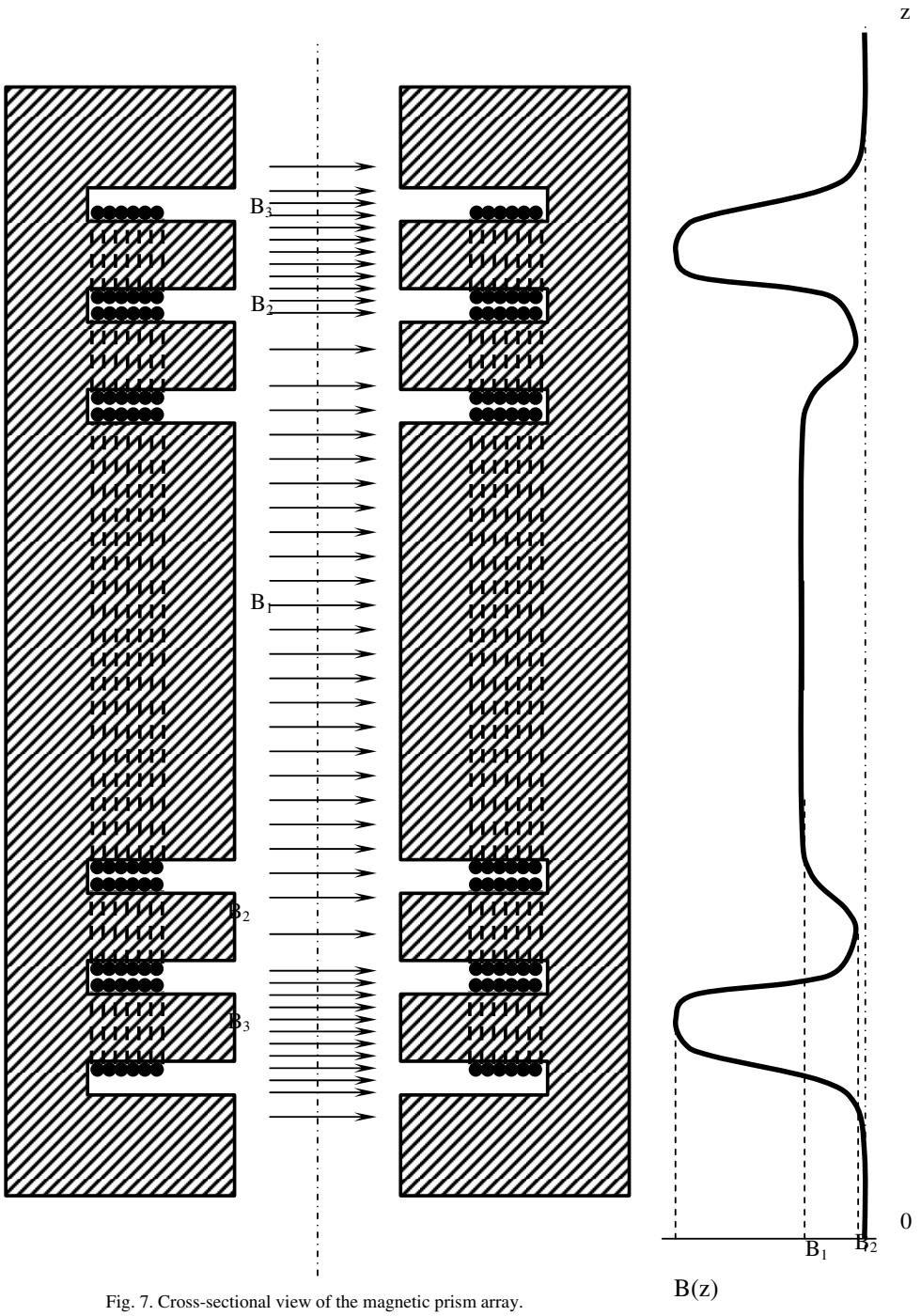

Fig. 7. Cross-sectional view of the magnetic prism array.

In an optimized prism array, each quadrant deflects the beam by 90° and transfers stigmatically two planes, the diffraction (slit) and (achromatic) image plane, with unit magnification. The excitations of the coils are chosen so that the prism behaves as a thick round lens along the curved axis and bends the beam by 90°. For a given flux density B_1 in the central polepiece, resulting in a deflection angle ϕ_1, there is a range of flux densities B_2 and B_3 such that the total deflection angle $\phi_1+\phi_2+\phi_3$ equals 90°, i.e. the ratio of B_2 and B_3 is variable. The fact that there are two separate coils generating flux densities B_2 and B_3 in each arm allows for effectively varying the length of the outer field and its center, thus correcting for potential machining and calculation errors and therefore allows electronic tuning of the prism exactly to its desired imaging condition. In addition, the fact that all the inner and outer sectors are independent allows the correction of machining errors that will result in a bending angle that is not exactly 90° for each quadrant and therefore allows the exact alignment of the beam in the objective, projection and illumination optics. The machining of the prism sectors is simplified by the sector shape with straight edges (no cuts at arbitrary angles or curved edges). The experimental realization of such a magnetic prism array is shown in Fig.8, and Fig. 9 shows that measured and simulated flux density along its symmetry axis are in good agreement. Experimental data obtained on a LEEM operating in photoemission at 30keV and equipped with a magnetic prism array are shown in Fig.10, demonstrating that large fields of view (2/3 of a mm) can be imaged by the prism without introducing significant aberrations.

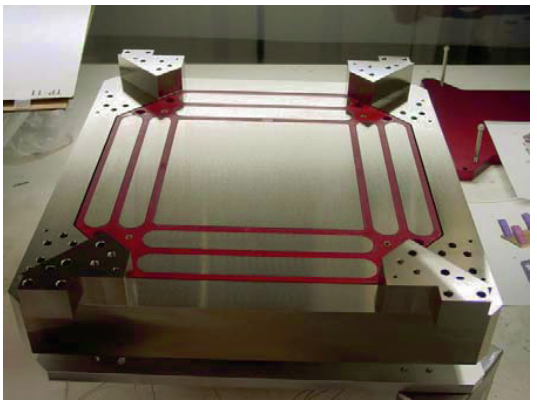

Fig. 8. Experimental realization of the magnetic prism array.

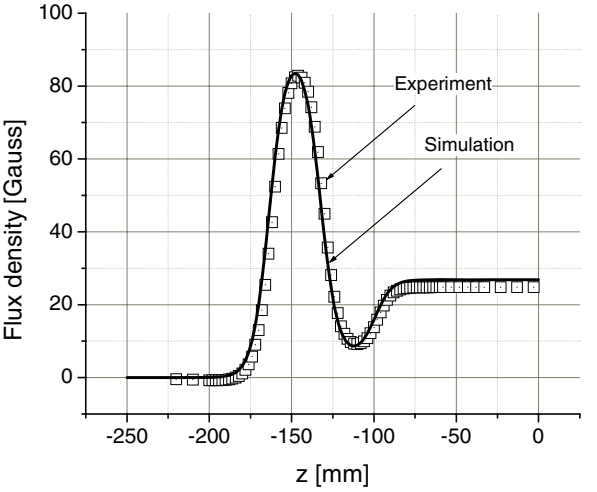

Fig. 9. Comparison of measured (squares) and simulated (solid line) flux density along the symmetry axis of the magnetic prism array.

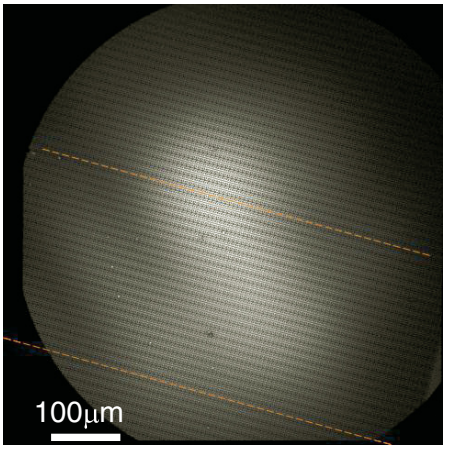

Fig. 10. Experimental photoemission image after 90 degree deflection by the magnetic prism array. Note: The field of view is 670 μm, and the two parallel dashed lines are meant to aid the assessment of distortions in the image. The intensity variations across the field of view are due to the non-symmetric laser spot. Sample: Aluminium-coated Si substrate with periodic, 100nm thick SiO_2 structures.

4. Illumination optics and 'twist' correction

The immersion nature of the objective lens strongly impacts the design of the illumination optics, in particular for the mirror mode. In the mirror electron microscopy imaging mode, when the wafer is biased near the potential of the electron source, the illuminating electrons are reflected above the surface, without hitting the surface. In order to obtain high spatial resolution, the electrons must turn around just several nanometers above the surface. In a magnetic immersion objective lens, this can be achieved at points near the optical axis. However, at points further from the optical axis, the electrons acquire a 'twist', i.e. the electrons' angular velocities in the magnetic field cause them to have circumferential kinetic energies at the turning point, which are proportional to the square of their off-axis distances. The total energy of the electron is conserved, so the axial energy component is reduced. As a result, the distance of the turning point from the wafer increases, as demonstrated in Fig. 11, causing a serious degradation of resolution, particularly for large fields of view.

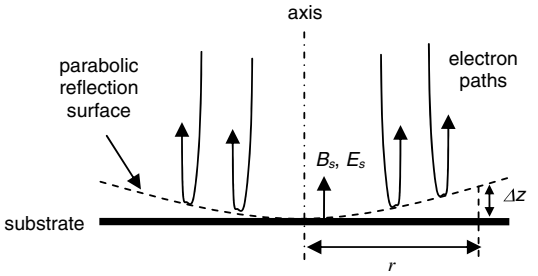

Fig. 11. Electron trajectories of mirror electrons near the substrate in a magnetic immersion lens.

This effect can be explained in terms of conservation of the canonical angular momentum $L_\Phi = m_e r^2 \omega + erA_\Phi$ in rotationally symmetric fields, where m_e is the electron mass, r is the off-axis distance, ω is the angular velocity, e is the electron charge and A_Φ is the angular component of the vector potential. Near the optical axis, $2\pi r A_\Phi = \pi r^2 B_s$ due to $\vec{B} = \nabla \times \vec{A}$, where B_s is the axial magnetic flux density at the surface. This means that a particle entering a rotationally symmetric field will acquire an angular momentum, which is lost again when leaving the field. On the other hand, a particle emitted from rest in a magnetic field will attain the angular momentum once it leaves the field (as it is the case in the previously described immersion objective lens). The canonical angular momentum at the substrate surface can then be calculated as

$$L_\Phi = m_e r^2 \omega + \tfrac{1}{2} e B_s r^2, \tag{1}$$

assuming that the radial velocity component is negligible. Consider now the complete illumination beam path of the electrons, starting from the gun cathode. When electrons are emitted from the cathode with no magnetic field and negligible emission velocity at the source surface, $L_\Phi = 0$. Due to momentum conservation, the electrons then will be precessing at the surface with a Larmor angular velocity ω,

$$\omega = -\frac{eB_z}{2m_e}. \tag{2}$$

The circumferential velocity $v = r\omega$ creates a circumferential kinetic energy $W_{k\Phi}$ (in electron Volts) at the reflection point, given by

$$W_{k\Phi} = \frac{1}{2}\frac{mv^2}{e} \tag{3}$$

When the focusing is adjusted so that there is no radial velocity at the turning point, then the quantity $W_{k\Phi}$ is the total kinetic energy at the turning point. This combines with the axial electric field E_z at the wafer surface to give a turning point height Δz of

$$\Delta z = \frac{W_{k\Phi}}{E_z} \quad , \tag{4}$$

assuming that electrons travelling along the axis just touch the surface, as shown in Fig. 11. For B_s = 0.1 Tesla and E_s = 5 kV/mm at the substrate surface, and $e/m = 1.7588\times10^{11}$ C/kg and an off-axis distance of r = 50 μm, Eq. (2) gives a circumferential velocity of $v = 4.397\times10^5$ m/s, Eq. (3) yields $W_{k\Phi}$ = 0.55 eV, and Eq. (4) gives a turning point height of $\Delta z \approx 110$ nm. From the above equations, Δz is proportional to r^2, so given that $\Delta z \approx 110$ nm for r = 50 μm, the turning point heights for various off-axis distances are as summarized in Table 1. Assuming the resolution is not limited by aberrations in the imaging optics, the best attainable resolving power in mirror mode is roughly equal to the turning point height Δz. It can thus be seen from Table 1 that the resolving power degrades rapidly as the field of view is increased.

Table 1
Turning point height as a function of off-axis distance.

Off- axis distance r (μm)	Turning point height Δz (nm)
50	110
100	440
150	880
200	1760

In systems with rotationally symmetric magnetic fields, electrons typically have non-zero angular velocities inside the magnetic fields, and zero angular velocity outside the magnetic field. However, this situation can be modified if we can arrange for the electrons to have non-zero angular velocities when outside the magnetic field. This situation can be produced by immersing the cathode of the electron gun in a magnetic field. In this case, the electrons are emitted normal to the cathode, i.e. without angular velocity, inside the magnetic field, and when they emerge from the magnetic field they then have a finite angular velocity in the field free region. If the beam then passes back into a magnetic field, the angular velocity can be cancelled again inside the field. By appropriately matching the magnetic field at the cathode to the magnetic field at the wafer, it should be possible in principle to cancel the circumferential velocity at the wafer.

Assume that the electron is emitted from the cathode immersed in a radially symmetric field B_c with negligible initial velocity at an off-axis distance r_c, and thus the total momentum

$$L_\Phi = m_e r^2 \omega + \tfrac{1}{2} e B_c r^2 = \tfrac{1}{2} e B_c r_c^{\,2} \tag{5}$$

If we now require that at the substrate surface the electrons also have negligible radial and angular velocity,

$$L_\Phi = m_e r^2 \omega + \tfrac{1}{2} e B_s r^2 = \tfrac{1}{2} e B_s r_s^{\,2} \tag{6}$$

where r_s is the off-axis distance at the turn-around point above the surface. Again, from momentum conservation, we derive that the necessary condition for an electron emitted from the cathode with zero angular velocity to reach the substrate plane with zero angular velocity is that the quantity r^2B must have the same value at the substrate as at the cathode,

$$B_s r_s^2 = B_c r_c^{\,2}, \quad \text{or} \tag{7}$$

$$B_c = M^2 B_s, \tag{8}$$

where M is the linear magnification from cathode to substrate.

It turns out that due to the immersion nature of the gun, it is not necessary to image the cathode onto the surface, and the more preferable gun crossover plane can be imaged. The system considered is shown in Fig. 12. Electrons emitted from the cathode C are focused by the gun lens G to form an image of the cathode at the plane of the field

lens *B*. This first image of the cathode is again focused by the field lens *A* to form a second image of the cathode at the objective back-focal plane (pupil) *P*. The gun crossover *X* is imaged by the field lens *B* to form a first image of the crossover at the plane of the field lens *A*, and the objective lens *O* forms a second image of the crossover at the substrate *W*. The distances between the various planes are denoted by L_{WP}, L_{PA}, L_{AB}, L_{BX} and L_{XC}, as indicated in Fig. 12. For simplicity, the gun region, *BXGC*, was simulated using the same structure and dimensions as the objective lens region, with the same magnetic field at the cathode surface. However, the geometry was reversed, and the cathode was biased 0.25 V more positive to prevent most of the electrons emitted from the cathode from hitting the substrate. At the cathode, the emission conditions assumed were a Maxwell-Boltzmann energy distribution, $p(E)dE = C.E.\exp(-E/E_0).dE$, with an energy width parameter $E_0 = 0.25$ eV, and a Lambertian ($\cos\theta$) angular intensity distribution. Trajectories were computed for various values of the distance L_{AB} between field lens *A* and field lens *B*. Varying the distance L_{AB} alters the magnification of the crossover *X* at the substrate plane *W*. For each value of the distance L_{AB}, the excitation of field lens *A* was adjusted to focus the plane Z_B at the plane Z_P, and the excitation of field lens *B* was adjusted to focus the plane Z_X at the plane Z_A.

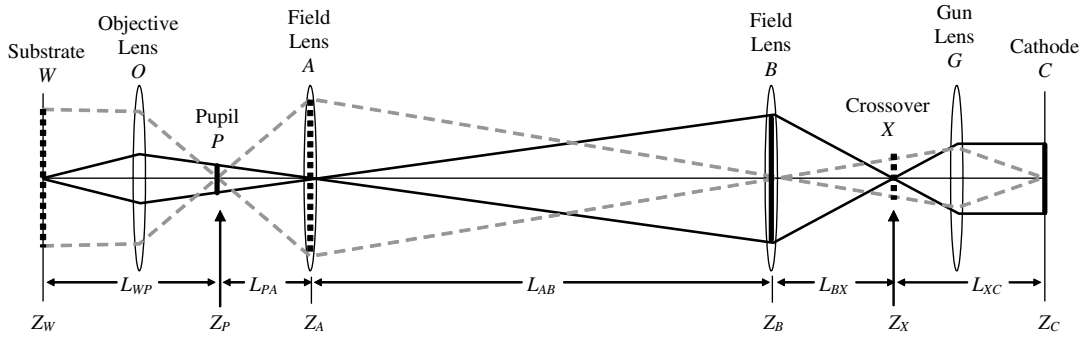

Fig. 12. Electron-optical diagram of twist-corrected illumination.

Results for four values of L_{AB} (175 mm, 225 mm, 350 mm, and 700mm) are plotted in Figs. 13a-d. In each case, the magnification M_{XW} between crossover and substrate was computed, and for each particle the axial height above the substrate and the total kinetic energy at the turning point were plotted. The circumferential and radial components of the kinetic energy of each particle at the turning point were also plotted. The values of these parameters at 250 μm off axis were estimated from these plots, and their values are indicated in the captions of the plots. These data are summarized in Table 2.

These results show that, when $L_{AB} = 225$ mm, for which the crossover is imaged at the substrate with unity magnification (i.e. $M_{XW} \approx 1$), then the values of axial height and total kinetic energy are effectively reduced to the values corresponding to the thermal energy distribution of the beam. At this condition, the illumination optics is considered to be twist-corrected, in agreement with equation (8). An experimental demonstration of this effect is shown in Fig. 13e, which compares mirror images obtained with a twist-corrected (right) and uncorrected (left) condition. The sample is a (100) p-type production quality Si test wafer with a 100nm thick thermally grown SiO_2, with a variety of patterns etched into the oxide layer using standard lithographic techniques, and the field of view is approximately 500μm. In the right image, the illumination lens settings are optimized for maximum field of view; while in the right image all the lenses are unchanged except the immersion gun lens, which is reversed in polarity, thus demonstrating the compensation of the circumferential velocity components at the wafer surface.

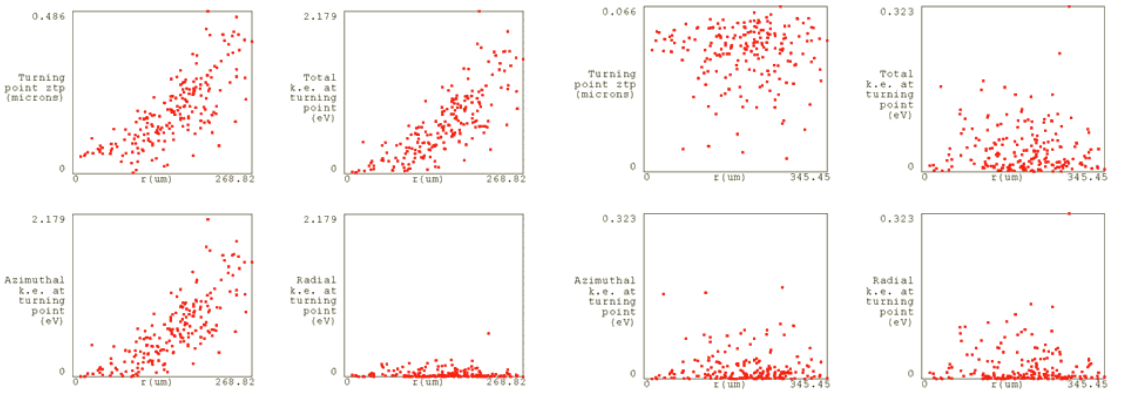

(a) L_{AB} = 175 mm M_{XW} = 0.776 E = 1.89 eV h = 420 nm

(b) L_{AB} = 225 mm M_{XW} = 0.998 E = 0.18 eV h = 66 nm

(c) L_{AB} = 350 mm M_{XW} = 1.552 E = 1.31 eV h = 314 nm

(d) L_{AB} = 700 mm M_{XW} = 3.103 E = 2.49 eV h = 563 nm

Fig. 13a-d. Results for "twist fix" correction, for various distances L_{AB} between the field lenses. In each case, M_{XW} = magnification between crossover and substrate, E = total kinetic energy at turning point 250 μm off axis, and h = height at turning point 250 μm off axis.

Table 2
Optical parameters as functions of the distance L_{AB} between the field lenses A and B.

L_{AB} (mm) (Distance between field lenses A and B)	M_{XW} (Magnification from crossover to wafer)	z_{tp} (nm) (height above wafer at turning point)	W_k (eV) (kinetic energy at turning point)
175	0.776	420	1.89
225	0.998	66	0.18
350	1.55	314	1.31
700	3.10	563	2.49

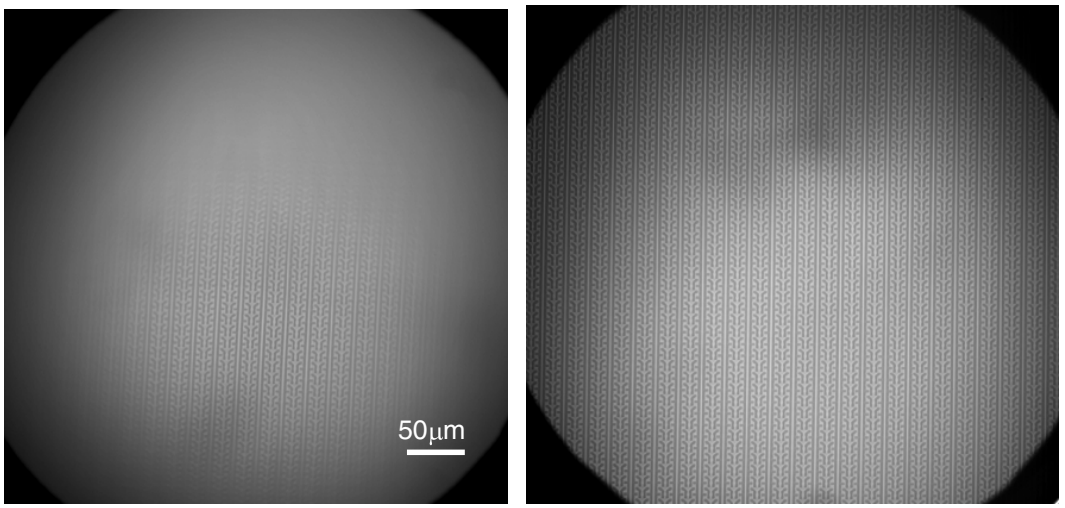

Fig. 13e. Experimental confirmation of twist fix. Right image – mirror image optimized for maximum field of view; left image – mirror image with all lenses unchanged except the immersion gun lens, which is reversed in polarity.

5. Dual beam approach

The dual beam approach is driven by the difficulties encountered when electron microscopes are used to image insulating surfaces. The imbalance between the arriving and leaving flux of electrons causes the surface to charge up, resulting in increased blur and distortions. On a homogeneous insulator surface, the charging can be suppressed by operating at a landing energy resulting in a net secondary yield of 1. However, this approach restricts the landing energy and typically does not work when different insulating materials are present at the surface. We have developed a dual beam approach that mitigates the charging effect when two electron beams with different landing energies are used for imaging [16]. The energy spectrum of the illuminating electrons approaching the substrate surface and signal electrons leaving the surface is shown in Fig.14a. Assume that the electron energy has a Maxwell-Boltzmann distribution peaked at 0.25 eV with a full-width-half-maximum of approximately 0.5 eV. The first beam is partially mirrored and backscattered (which does not charge up the surface), and its high energy tail is absorbed, which charges the surface negatively. For simplicity, the small fraction of backscattered electrons is not shown in Fig.14. The second beam strikes the wafer with energies of typically few hundred eV, which results in a total (secondary and backscattered) yield $\sigma = \delta + \eta$ larger than 1 that charges the surface positively. Assuming that the portion of the mirror beam current I_m that is absorbed equals to αI_m, and the second, charge control beam current equals to I_{cc}, the condition for charge equilibrium then can be written as

$$\alpha I_m = (\sigma - 1) I_{cc} \tag{9}$$

This state of charge control is a dynamic quasi-equilibrium, and the surface is at a potential that is slightly (<1eV) more negative than the cathode potential (0V), depending on the fraction of absorbed mirror electrons. This is demonstrated in Fig. 14b. When the charge control beam current I_{cc1} (or total yield σ) slightly increases, the surface begins to charge positively, thus attracting the mirror beam, and a slightly larger number of mirror beam electrons will get absorbed, returning the insulating surface to a charge equilibrium at a slightly less negative potential U_{s1} when compared to the cathode potential. Similarly, when the charge control beam current I_{cc2} (or total yield σ) slightly decreases, the surface begins to charge negatively, which repels the mirror beam, and a slightly smaller number of mirror beam electrons will get absorbed, returning the insulating surface to a charge equilibrium at a slightly more negative potential U_{s2} when compared to the cathode potential. The potential variation is expected to be small and is greatly exaggerated in Fig. 14b, considering the small width and steep slope of the energy distribution and the typical emission stability achieved with electron sources (<1%).

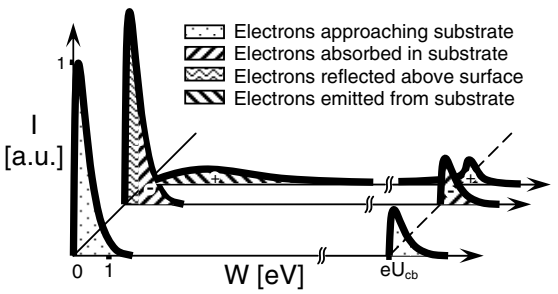

Fig..14a. Energy spectrum of illuminating electrons approaching the substrate surface and signal electrons leaving the surface, U_{cb} - relative cathode bias.

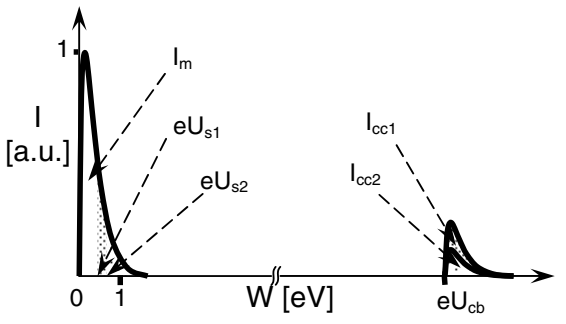

Fig..14b. Energy spectrum of electrons for two different charge control currents.

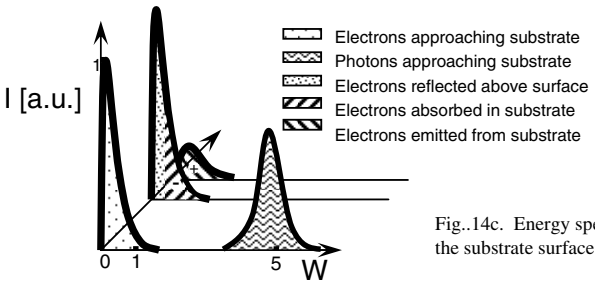

Fig..14c. Energy spectrum of illuminating electrons and photons approaching the substrate surface and signal electrons leaving the surface.

Another possible dual beam approach that mitigates the charging effect involves a mirror electron beam combined with a bright UV laser beam [17]. The energy spectrum of the illuminating electrons and photons approaching the substrate surface, and signal electrons leaving the surface, is shown in Fig.14c. As in the previous case, we assume that the electron beam is partially mirrored and backscattered (which does not charge up the surface) and its high energy tail is absorbed, which charges the surface negatively. We use a 266nm UV laser that has photons with a wavelength corresponding to ~ 4.8eV, which results in a photoemission yield γ that charges the surface positively. Assuming that the portion of the mirror beam current I_m that is absorbed equals to αI_m, and the photoemission current equals to I_λ, the condition for charge equilibrium then can be written as

$$\alpha I_m = I_\lambda = \gamma P , \tag{10}$$

where P is the laser power needed to generate the required photoemission current I_λ and γ is the photoemission yield.

We have experimentally generated two independent electron beams in an electron gun equipped with two concentric cathodes, with the outer ring cathode biased negatively by a few hundred volts with respect to the inner disc cathode. Both beams pass through the same illumination optics and are refocused at the substrate to form overlapping dual-beam illumination. The geometry of the dual beam gun is shown in Fig. 15a, and a detail of the raytrace near the cathode surface for both beams is shown in Fig. 15b. Both cathodes are of the barium dispenser type, heated to approximately 1000^o C. The cathodes are surrounded by a steering, focusing and shield electrode and a beam-limiting aperture is located in the grounded anode. The shield electrode is added between the steering electrode and anode to prevent arcing and its potential is the same as the potential of the inner cathode. The ratio of the currents can be set by either varying the individual cathode temperatures or by a combination of bias voltages applied to the first two electrodes surrounding the cathodes. Fig. 16 illustrates the experimental overlap of the two beams on the substrate and the adjustment of their current ratio by varying the voltages of the steering and focus electrodes.

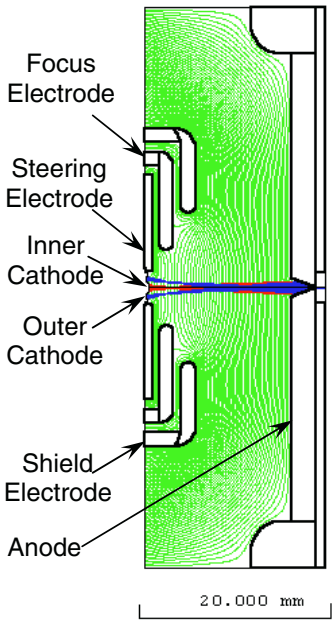

Fig. 15a (left). Overall view of the dual beam gun geometry with trajectories and equipotentials (V_{focus} = −27 kV and $V_{steering}$ = −30.15 kV).

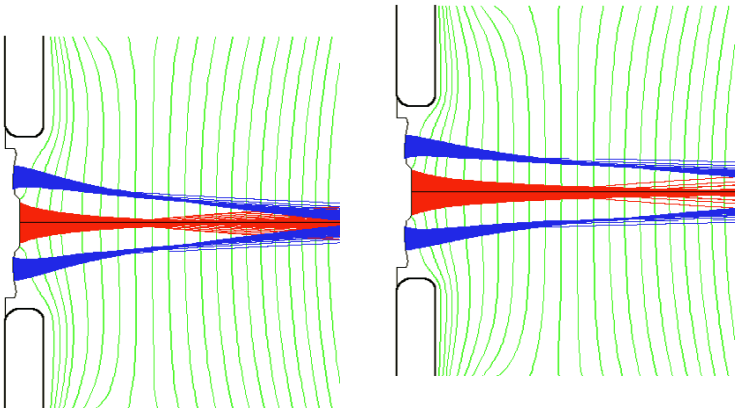

V_{focus} = −27 kV and $V_{steering}$ = −30.15 kV. V_{focus} = −26 kV and $V_{steering}$ = −30.00 kV.

Fig. 15b (above). Enlarged view of trajectories and equipotentials near the cathode demonstrating the effect of the steering and focus electrodes.

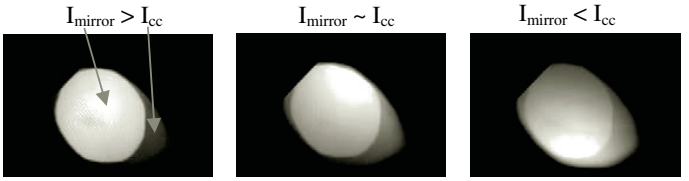

Fig.16. Substrate illumination with two beams and varying mirror-to-charge control beam current, mirror beam diameter is approximately 150μm.

The experimental verification of the dual beam charge control approach is demonstrated in Fig. 17a. The sample is a (100) p-type production quality Si test wafer with a 100nm thick thermally grown SiO_2, with a variety of patterns etched into the oxide layer using standard lithographic techniques. When the substrate is illuminated solely with the lower energy mirror beam with a landing energy close to 0 eV, the oxide charges negatively and the image appears blurred. Similarly, when the substrate is illuminated solely with the higher energy charge control beam with a landing energy of a few hundred eV, the oxide charges positively, and the resulting image appears blurred. However, when both beams are used to illuminate the substrate and their ratio is adjusted to obtain dynamic charge equilibrium, a crisp image is observed.

The experimental verification of the laser control approach is demonstrated in Fig. 17b. The sample is the same as in the previous case, i.e. a (100) p-type production quality Si test wafer with a 100nm thick thermally grown SiO_2, with a variety of patterns etched into the oxide layer using standard lithographic techniques. When the substrate is illuminated solely with the lower energy mirror beam with a landing energy close to 0 eV, the oxide charges negatively and the image appears blurred. Similarly, when the substrate is illuminated solely with the 266nm UV laser beam, the oxide charges positively, and the resulting image appears blurred. However, when the mirror electron and photon beams overlap, and their ratio is adjusted to obtain dynamic charge equilibrium, the charging-induced blur vanishes.

When normal landing of both beams at the wafer is required, an energy-dispersive device is needed to compensate for the difference in deflection angle between the mirror and charge control beam in the prism array. When the prism array is set to deflect the mirror beam by precisely 90^o ($\pi/2$ rad), the higher energy charge control beam is deflected by a slightly smaller angle, which for a 29.7 keV mirror beam and 30 keV charge control beam

amounts to approximately 5.1 mrad. We have chosen an omega filter located in the illumination optics (Fig. 18) that introduces an angular dispersion between the lower energy mirror beam and the higher energy charge control beam, to cancel the angular dispersion in the prism. The general arrangement of the omega filter is shown schematically in Fig. 19. The angular dispersion between the mirror and charge control beams is 15.4 mrad for this particular design, which is approximately 3 times the angular dispersion of the magnetic prism. An accurate cancellation of the angular dispersion in the main prism is achieved by a set of transfer lenses with a variable magnification of ~ 3x. The computed image-to-slit distance, L, is 47.8 mm, and the focal length is given by $f = L/2 = 23.9$ mm. The omega filter is designed to operate as a field lens with a net magnification equal to 1, i.e. with the field rays imaged symmetrically about the mid-plane, between the diffraction and slit planes, as shown in Fig. 19.

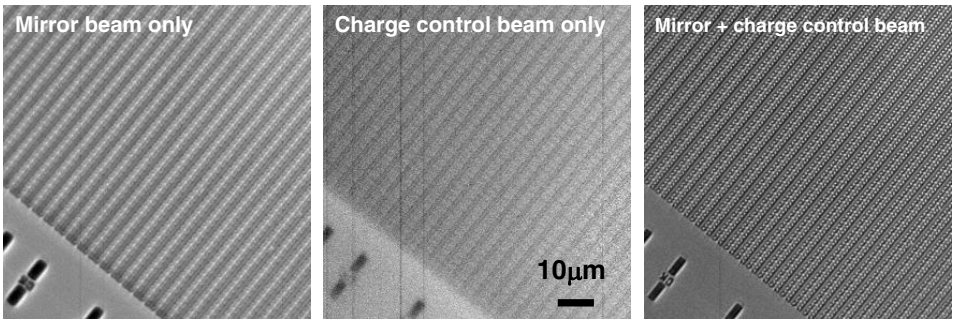

Fig. 17a. Demonstration of dual beam charge control on a Si substrate with periodic, 100nm thick SiO_2 structures. Left - mirror beam only (mirror mode); centre - image with charge control beam only (secondary electron mode); right - dual beam illumination adjusted to achieve charge control.

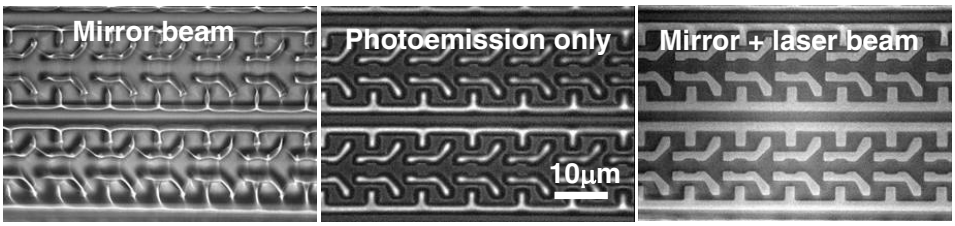

Fig. 17b. Demonstration of laser charge control on a Si substrate with periodic, 100nm thick SiO_2 structures. Left - mirror beam only (mirror mode); center – photoemission image only; right – overlapping mirror and laser beam illumination adjusted to achieve charge control.

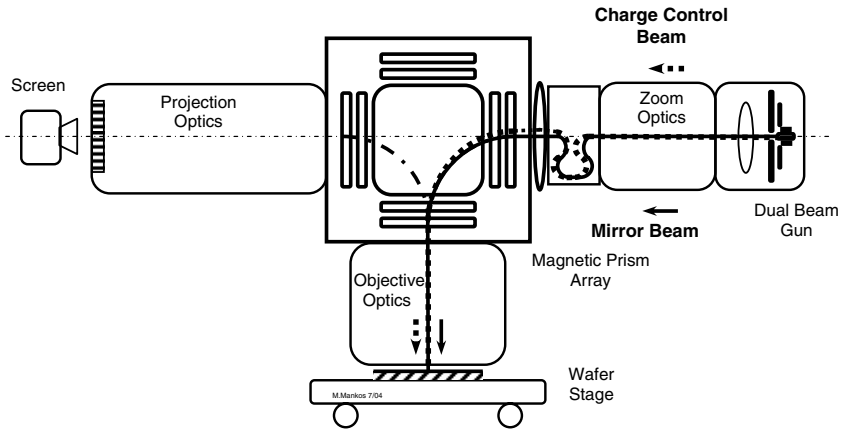

Fig. 18. Layout of dual beam column with omega filter.

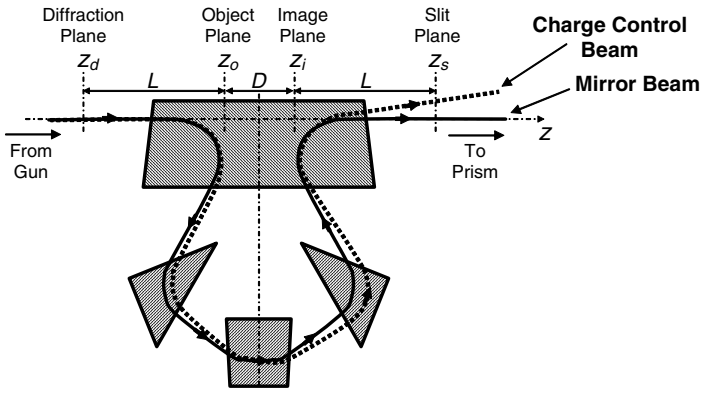

Fig. 19. Schematic diagram of the omega filter.

6. Tilted illumination optics

A LEEM can be operated in a variety of imaging modes utilizing secondary, backscattered (diffracted), mirrored and photoemission electrons [1,2]. We have found that imaging modes with tilted illumination can add additional valuable information about the sample. In particular, it can enhance topographic features due to the extended shadow, and on magnetic specimen it can reveal magnetic contrast.

In order to achieve a large deflection angle and maintain low aberrations, a small tilt angle is introduced in the illumination optics (Fig. 20). Due to the strong decelerating field at the substrate, this angle gets magnified by the square root of the ratio of the beam energy and landing energy, i.e. for a 30 keV beam energy and a landing energy of 3eV, the illumination angle at the biased wafer is 100x larger than in the remainder of the electron optics, where the electron have a 30 keV beam energy. For example, a small and easily achievable tilt angle of 0.45° (7.85mrad) gets magnified to a 45° landing angle. Therefore, a full range of landing angles from 0° to 90° is available, at an arbitrary azimuthal landing angle.

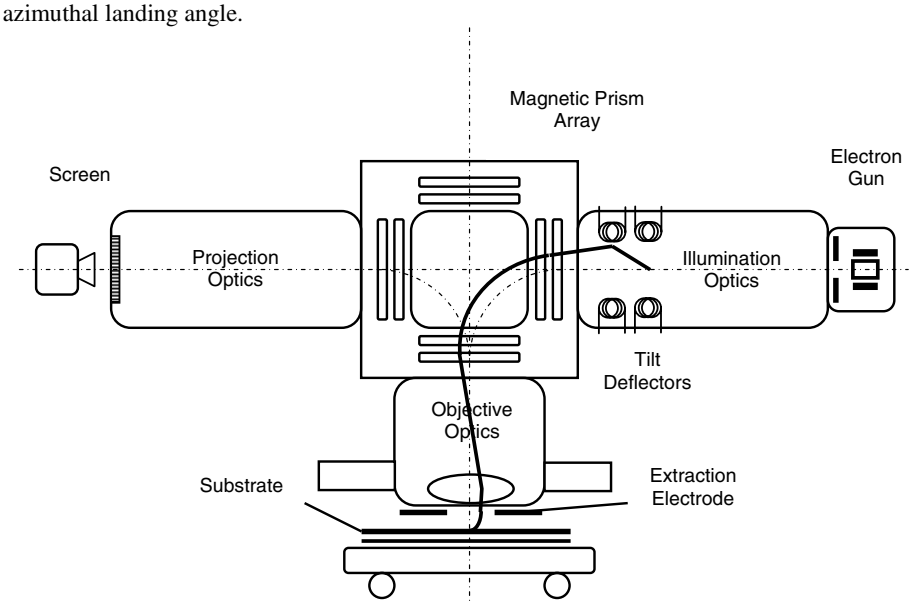

Fig. 20. Layout of electron-optical column with tilted illumination.

The tilted illumination mode can significantly increase the contrast of topographical features. This is caused by the shadowing effect (Fig.21) of the tilted illumination: areas in the shadow of the feature do not emit or reflect any electrons, and the illumination side of the defect has enhanced emission due to the capture of illuminating electrons on the side wall. With increasing tilt angle, the shadow extends further and the signal becomes stronger when compared to images with normal incidence of illuminating electrons. This technique allows achieving large beam tilts at the sample with the same spatial resolution as with zero tilt without using a tilting stage, which is necessary in conventional scanning and transmission electron microscopes. The azimuthal direction of the tilted illuminating beam can be easily determined by analyzing the shadows in the image. An experimental example of this imaging mode, shown in Fig. 22, compares the contrast obtained with normal incidence (top) and illumination tilted to 70° (bottom). The sample is an aluminium-coated (100) p-type production quality Si test wafer with a 100nm thick thermally grown SiO_2, with a variety of patterns etched into the oxide layer using standard lithographic techniques. The small particle in the upper right of the images is clearly more discernable in the image with large tilt, and no degradation in spatial resolution is observed. The height of the periodic pattern is 100nm, and from the ratio of the shadow lengths one can deduce that the particle is approximately 800nm high.

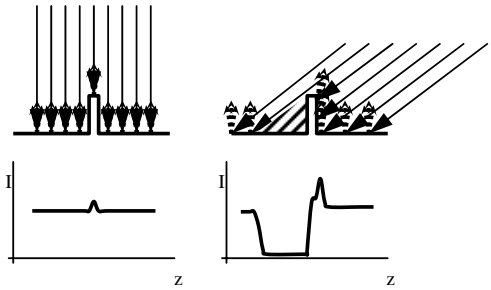

Fig. 21. Schematic electron trajectories and intensity profiles for normal (left) and tilted (right) beam incidence.

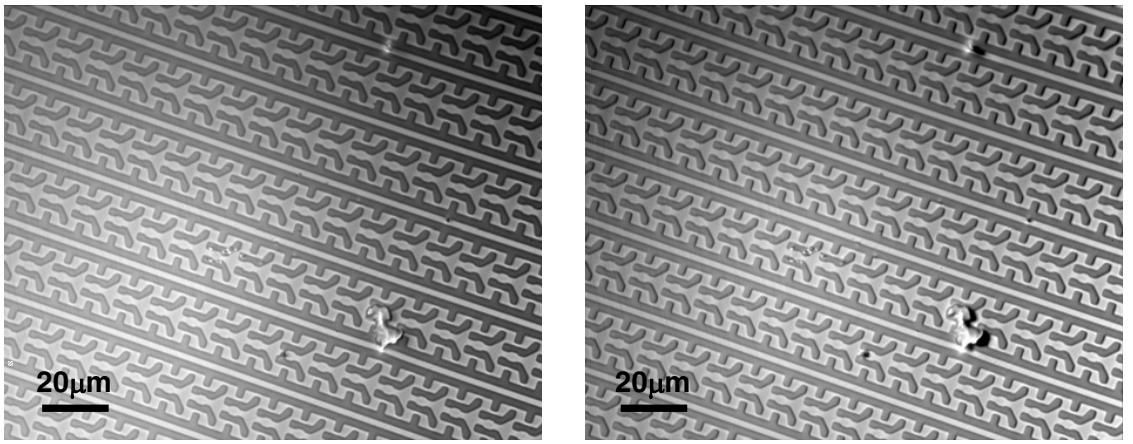

Fig. 22. Imaging with tilted illumination. Left – normal incidence (0 degrees); Right – 70 degree incidence angle; sample: Aluminium-coated Si substrate with periodic, 100nm thick SiO_2 structures.

Tilted illumination can also reveal the magnetic microstructure on the surface of magnetic substrates [18, 19]. We have used tilted illumination to reveal the magnetic contrast associated with bits of stored information on commercially available magnetic recording media. The observed magnetic contrast can be explained classically using the Lorentz force acting on electrons moving in a magnetic field. As the electrons slow down while approaching the surface, the magnetic flux leaking above the sample deflect the electrons. When the electron beam

is normal to the surface of a magnetic sample, deflection due to magnetic fields in the illuminating and imaging paths cancels and only topographical information is obtained. However, when the beam is tilted, the deflection due to the magnetic fields is additive in the illuminating and imaging paths and reveals the magnetic structure. The focus, sample bias and tilt can be then adjusted to maximize the magnetic contrast.

Fig. 23 depicts images obtained from a magnetic hard disk and have a field of view 80 μm wide. The image on the left was obtained using a tilted incident beam and shows predominantly magnetic contrast. The bias on the specimen is set near the mirror condition and focusing by the objective lens was adjusted to obtain maximum contrast. The horizontal lines represent magnetic bits recorded onto the hard disk prior to the experimental viewing. Larger period bits on the left side are spaced approximately 3 μm apart, smaller period bits on the right side are spaced approximately 1.8 μm apart. The right image, showing the same area of the same specimen as in the left image, was obtained using a beam normal to the surface and displays predominantly topographical contrast. The group of surface defects marked by arrows can be clearly distinguished in both images, thus allowing the correlation of magnetic and surface microstructure.

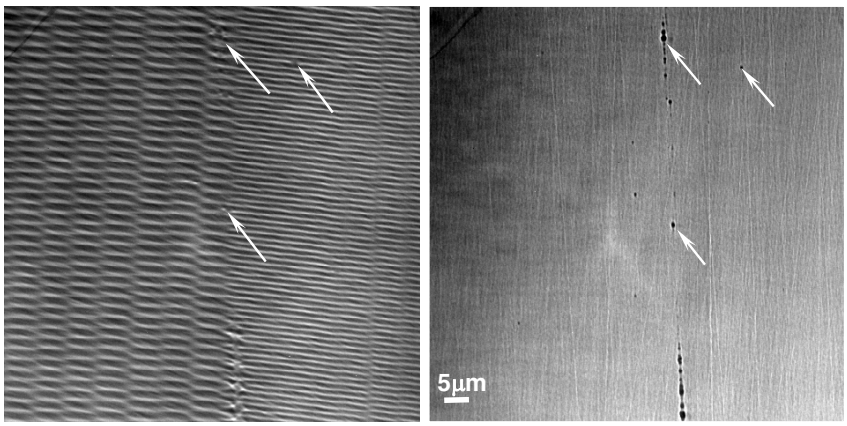

Fig. 23. Imaging of data stored on magnetic recording media (hard disk). Left – tilted illumination reveals magnetic microstructure associated with individual bits; right – normal incidence reveals topographic contrast only. Note: The arrows mark the same defects in both images.

The strong magnetic contrast enables a variety of magnetic specimen, i.e. magnetic media and read/write heads, to be inspected at high throughput and high resolution.

This is a significant advantage compared to other electron-optical methods used for high resolution imaging of magnetic contrast, as most of the existing light- and electron-optical imaging techniques have either important resolution or throughput limitations. The most widely used electron-optical techniques, Lorentz transmission microscopy and electron holography [20] require thin substrates. For bulk specimen, secondary (type I contrast) or backscattered electrons (type II contrast) can be utilized in a scanning electron microscope (SEM) for magnetic imaging, however the contrast is usually extremely low. Scanning electron microscopy with polarization analysis (SEMPA, [21]), which uses a spin analyzer to detect the excited spin-polarized secondary electrons, requires very long exposure times and costly instrumentation. In spin-polarized low energy electron microscopy (SPLEEM, [22]), where the sample is illuminated with a spin-polarized beam and the contrast arises from the exchange scattering between the incident and sample electrons, expensive instrumentation and low intensity of the polarized electron source limit the high-throughput applications of this technique. The combined high throughput, high resolution tilted-illumination mirror electron microscopy approach has a potential to satisfy magnetic imaging applications requiring high spatial resolution and high imaging speed at a reasonable instrumentation cost.

7. Conclusions

We have developed several novel electron-optical components and concepts that improve the throughput and extend the applications of a LEEM. When the substrate is immersed in the magnetic field of the cathode objective lens, a substantial reduction in the e-e interactions and the associated blur can be seen when compared to conventional purely electrostatic and non-immersion magnetic lenses. The immersion nature of the objective lens introduces a twist in the mirror mode, which causes a serious degradation of resolution. This twist effect vanishes when the cathode of the electron gun is immersed in a rotationally symmetric magnetic field that is appropriately matched to the magnetic field at the substrate. The charging effects encountered when a LEEM is used to image insulating surfaces can be mitigated when two illumination electron beams with different landing energies are used. A similar effect can be obtained when a partially mirrored beam and overlapping UV beam are used. We have demonstrated experimentally a LEEM with two independent electron beams using an electron gun equipped with two concentric cathodes, and obtained images free of charging artifacts. Similar results were obtained when a laser beam was used to mitigate the charging effects. When normal landing of both beams at the wafer is needed, a energy-dispersive device (i.e. omega filter) is needed to compensate for the difference in deflection angle in the prism array. We have experimentally demonstrated imaging modes with tilted illumination allowing a large range of tilt angles from perpendicular to glancing without loss of resolution. At or near glancing incidence, large shadows are formed on even the smallest topographic features, easing their detection. On magnetic substrates, we have observed magnetic microstructure in magnetic media with high throughput and resolution.

Acknowledgements

This project was funded by DARPA under Contract No. DAAD19-003-1010, “Advanced Lithography Development”. The authors would like to thank DARPA for providing funding for this work, and Xieqing Zhu, John Rouse and Haoning Liu of MEBS Ltd. for help and fruitful discussions, and D. Soltz and H. Hess for numerous contributions to the magnetic contrast studies.

References

[1] W. Telieps and E. Bauer, Ultramicroscopy 17 (1985) 57.
[2] R.M. Tromp and M.C. Reuter, Ultramicroscopy 50 (1993) 171.
[3] G.F. Rempfer, W.P. Skoczylas, O. H. Griffith, Ultramicroscopy 36 (1991) 196.
[4] R.N. Watts et al., Rev. Sci. Instrum 68 (1997) 3464.
[5] I. Mullerova, Scanning 23 (2001) 379.
[6] W.D. Meisburger, A.D. Brodie and A.A. Desai, J. Vac. Sci. Technol. B 10 (1992) 2804.
[7] M. Miyoshi, Y. Yamazaki, T. Nagai and I. Nagahama, J. Vac. Sci. Technol. B 17 (1999) 2799.
[8] M. Mankos et al., J. Vac. Sci. Technol. B 18 (2000) 3010.
[9] M. Mankos et al., J. Vac. Sci. Technol. B 19 (2001) 467.
[10] G.H. Jansen, J. Appl. Phys. 84 (1998) 4549.
[11] M.M. Mkrtchyan, J.A. Liddle, S.D. Berger and L.R. Harriott, J. Appl. Phys. 78 (1995) 6888.
[12] M. Mankos, A. Sagle, S.T. Coyle and A. Fernandez, J. Vac. Sci. Technol. B 19 (2001) 2566.
[13] M. Mankos and D. Adler, Ultramicroscopy 93 (2002) 347.
[14] V. Kolarik, L.H. Venklasen and M. Mankos, Optik 87 (1991) 1.
[15] R. Degenhardt, Ph.D. Dissertation, Technische Hochschule Darmstadt (1992).
[16] L. Veneklasen and D.L. Adler; U.S. Patent # 6,586,733, July 1, 2003.
[17] D.L. Adler and M. Marcus; U.S. Patent # 6,979,819, December 27, 2005.
[18] H. Mayer, J. Appl. Phys 28 (1957) 975.
[19] M. Mankos, D.A. Soltz and H.F. Hess, U.S. Patent # 6,936,816, August 30, 2005.
[20] M. Mankos, M.R. Scheinfein and J.M. Cowley, Advances in Imaging and Electron Physics 98 (1996) 323.
[21] M.R. Scheinfein, J. Unguris, M.H. Kelley, P.T. Pierce, R.J. Celotta, Rev. Sci. Instrum. 61 (1990) 2501.
[22] M.S. Altman, H. Pinkvos, J. Hurst, H. Poppa, G. Marx and E. Bauer, Mat. Res. Soc. Symp. Proc. 232 (1991) 125.